Nada: A new code for studying self-gravitating tori around black holes

Pedro J. Montero,[1] José A. Font,[1] and Masaru Shibata[2]

[1]*Departamento de Astronomía y Astrofísica, Universidad de Valencia, Dr. Moliner 50, 46100 Burjassot, Spain*
[2]*Graduate School of Arts and Sciences, University of Tokyo, Komaba, Meguro, Tokyo 153-8902, Japan*

We present a new two-dimensional numerical code called Nada designed to solve the full Einstein equations coupled to the general relativistic hydrodynamics equations. The code is mainly intended for studies of self-gravitating accretion disks (or tori) around black holes, although it is also suitable for regular spacetimes. Concerning technical aspects the Einstein equations are formulated and solved in the code using a formulation of the standard $3 + 1$ Arnowitt-Deser-Misner canonical formalism system, the so-called Baumgarte-Shapiro Shibata-Nakamura approach. A key feature of the code is that derivative terms in the spacetime evolution equations are computed using a fourth-order centered finite difference approximation in conjunction with the Cartoon method to impose the axisymmetry condition under Cartesian coordinates (the choice in Nada), and the puncture/moving puncture approach to carry out black hole evolutions. Correspondingly, the general relativistic hydrodynamics equations are written in flux-conservative form and solved with high-resolution, shock-capturing schemes. We perform and discuss a number of tests to assess the accuracy and expected convergence of the code, namely, (single) black hole evolutions, shock tubes, and evolutions of both spherical and rotating relativistic stars in equilibrium, the gravitational collapse of a spherical relativistic star leading to the formation of a black hole. In addition, paving the way for specific applications of the code, we also present results from fully general relativistic numerical simulations of a system formed by a black hole surrounded by a self-gravitating torus in equilibrium.

I. INTRODUCTION

Self-gravitating tori (or thick accretion disks) orbiting black holes (BHs) are common end-products in a number of scenarios of relativistic astrophysics. Theoretical evolutionary paths predict that they may form after the merger of a binary system formed by a BH and a neutron star (NS) or the system formed by two NS (see e.g. [1] and references therein). In addition, they may also be the result of the gravitational collapse of the rotating core of massive stars [2,3]. State-of-the-art numerical simulations have started to provide quantitative estimates of the viability of such systems to form [1,4–14]. Furthermore, such a thick disk plus BH system is thought to be the central engine for gamma-ray bursts [15–18]. Therefore, understanding the formation and dynamics of such systems is a highly relevant enterprise, along with discerning its stability properties. Namely, whether they may be subject to axisymmetric and nonaxisymmetric instabilities which could also lead to the emission of a significant amount of gravitational radiation.

In particular, the so-called runaway instability, first found by Abramowicz, Calvani and Nobili [19], is an axisymmetric instability that could destroy the torus on dynamical timescales. The numerical study of the runaway instability in general relativity has so far been investigated under different assumptions and approximations (see e.g. [20,21] and references therein). Despite that some progress has been made, the existing works are not still conclusive

on the likelihood of the instability, mainly due to the absence of important physics in the modeling. The complexity of handling the presence of a spacetime singularity in addition to the (magneto-)hydrodynamics and the self-gravity of the (possibly magnetized) accretion torus, turn very challenging the task of carrying out full general relativistic simulations of BH surrounded by a self-gravitating torus. The code we present in this paper is built with this midterm goal in mind.

Numerical studies of the dynamics of matter around BHs are abundant in the literature (see e.g. the references reported in [22]). For the kind of specific work we discuss in this paper we note, in particular, that [23,24] already focused on the numerical evolution of matter in dynamical axisymmetric BH spacetimes. Recent developments in numerical relativity associated with the puncture method for evolving BHs [25,26] have proved essential to perform accurate and long-term stable evolutions of spacetimes containing BHs, and the first successful simulations of BH/BH binaries have only been possible very recently (see [27] and references therein). Shibata [13,14] used the puncture method to investigate the merger of BH/NS binary system in full general relativity, and Faber *et al.* [28] considered relativistic spherical accretion onto a BH. In addition, Baiotti and Rezzolla [29] were also able to handle the accretion of matter onto a newly formed BH resulting from the collapse of a rotating NS without needing to excise the singularity.

In order to take advantage of this approach, Shibata [30] presented a formulation for computing equilibrium configurations of a BH and a self-gravitating torus in the puncture framework. Previous computations of this system by Nishida and Eriguchi [31], and also by Ansorg and Petroff [32] were not done in the puncture framework. In this paper we use the initial data in the formalism presented in [30] to carry out the first dynamical simulations of a self-gravitating torus in equilibrium around a BH as a first step towards a systematic investigation of the runaway instability in full general relativity. Such initial data are evolved using a new two-dimensional, general relativistic hydrodynamics code called Nada which is presented and thoroughly tested in this paper. As we explain in detail below our code solves the $3 + 1$ Einstein equations using the formulation originally proposed by Nakamura [33] and subsequently modified by Shibata-Nakamura [34] and Baumgarte-Shapiro [35], which is usually known as the Baumgarte-Shapiro Shibata-Nakamura (BSSN) formulation. On the other hand, the general relativistic hydrodynamics equations are written in flux-conservative form and solved with a high-resolution shock-capturing scheme (HRSC) [22,36,37]. In addition, the Nada code implements the Cartoon method [38] which allows to impose the axisymmetry condition while still admitting the use of Cartesian coordinates, the puncture/moving puncture approach to deal with the BH singularity and derivative terms in the spacetime evolution equations are computed using a fourth-order centered finite difference approximation.

The code is written in FORTRAN 90, requires approximately 8 bytes of memory per grid point, and it takes about 200 microseconds per grid point per time step using a five stages Runge-Kutta (see section III) for the time integration on a 2.0 GHz AMD Opteron Dual Core 270.

The organization of the paper is as follows: the formulation of the Einstein equations, including the implementation of the puncture approach and gauge conditions, along with the formulation of the general relativistic equations is briefly presented in Section II. Section III gives a short description of the boundary conditions and numerical methods employed for the time evolutions. Section IV and V are devoted to present results from tests the code has passed, for vacuum and nonvacuum spacetimes, respectively. Section VI discusses numerical simulations of self-gravitating equilibrium tori, in preparation for subsequent work. A summary of our conclusions is given in Section VII. We use units in which $c = G = 1$, and in sections V C to V F we also use $M_\odot = 1$. Greek indices run from 0 to 3, Latin indices from 1 to 3, and we adopt the standard convention for the summation over repeated indices.

II. BASIC EQUATIONS

We give next a brief overview of the formulation for the system of Einstein and hydrodynamic equations as have been implemented in the code.

A. Formulation of Einstein equations

1. BSSN formulation

We follow the $3 + 1$ formulation in which the spacetime is foliated into a set of nonintersecting spacelike hypersurfaces. In this approach, the line element is written in the following form

$$ds^2 = -(\alpha^2 - \beta_i\beta^i)dt^2 + 2\beta_i dx^i dt + \gamma_{ij}dx^i dx^j, \quad (2.1)$$

where α, β^i and γ_{ij} are the lapse function, the shift three-vector, and the three-metric, respectively. The latter is defined by

$$\gamma_{\mu\nu} = g_{\mu\nu} + n_\mu n_\nu, \quad (2.2)$$

where n^μ is a timelike unit-normal vector orthogonal to a spacelike hypersurface.

A reformulation of the Arnowitt-Deser-Misner canonical formalism (ADM) system, the BSSN formulation [33–35], has been implemented to solve the Einstein equations. Initially, a conformal factor is introduced, and the conformally related metric is written as

$$\tilde{\gamma}_{ij} = e^{-4\phi}\gamma_{ij}, \quad (2.3)$$

such that the determinant of the conformal metric, $\tilde{\gamma}_{ij}$, is unity and $\phi = \ln(\gamma)/12$, where $\gamma = \det(\gamma_{ij})$. We also define the conformally related traceless part of the extrinsic curvature K_{ij},

$$\tilde{A}_{ij} = e^{-4\phi}A_{ij} = e^{-4\phi}\left(K_{ij} - \frac{1}{3}\gamma_{ij}K\right), \quad (2.4)$$

where K is the trace of the extrinsic curvature. After introducing these new variables, the evolution equations can be expressed as

$$(\partial_t - \mathcal{L}_\beta)\phi = -\frac{1}{6}\alpha K, \quad (2.5)$$

$$(\partial_t - \mathcal{L}_\beta)K = -\gamma^{ij}D_j D_i\alpha + \alpha\tilde{A}_{ij}\tilde{A}^{ij} + \frac{1}{3}\alpha K^2 + 4\pi\alpha(E + S), \quad (2.6)$$

$$(\partial_t - \mathcal{L}_\beta)\tilde{\gamma}_{ij} = -2\alpha\tilde{A}_{ij}, \quad (2.7)$$

$$(\partial_t - \mathcal{L}_\beta)\tilde{A}_{ij} = e^{-4\phi}(-D_i D_j\alpha + \alpha(R_{ij} - 8\pi S_{ij}))^{\mathcal{TF}} + \alpha(K\tilde{A}_{ij} - 2\tilde{A}_{il}\tilde{A}^l_j), \quad (2.8)$$

$$\partial_t\tilde{\Gamma}^i = -2\tilde{A}^{ij}\partial_j\alpha + 2\alpha\left(\tilde{\Gamma}^i_{jk}\tilde{A}^{jk} - \frac{2}{3}\tilde{\gamma}^{ij}\partial_j K - 8\pi\tilde{\gamma}^{ij}S_j + 6\tilde{A}^{ij}\partial_j\phi\right) + \beta^j\partial_j\tilde{\Gamma}^i - \tilde{\Gamma}^j\partial_j\beta^i + \frac{2}{3}\tilde{\Gamma}^i\partial_j\beta^j + \frac{1}{3}\tilde{\gamma}^{li}\partial_{jl}\beta^j + \tilde{\gamma}^{lj}\partial_{lj}\beta^i, \quad (2.9)$$

where $\tilde{\Gamma}^i_{jk}$ are the connection coefficients associated with

$\tilde{\gamma}_{ij}$, $\mathcal{L}_\beta$ refers to the Lie derivative along the shift vector (see e.g. [39] for the tensor weights necessary to evaluate the Lie derivatives), and D_i and R_{ij} are the covariant derivative operator and the three-dimensional Ricci tensor associated with the three-metric γ_{ij}, respectively. The object $\tilde{\Gamma}^i$, known as the *conformal connection functions*, is defined as

$$\tilde{\Gamma}^i \equiv \tilde{\gamma}^{jk}\tilde{\Gamma}^i_{jk} = -\partial_j \tilde{\gamma}^{ij}. \tag{2.10}$$

The Ricci tensor R_{ij} that appears in the source term of the evolution Eq. (2.8) is split into two parts as follows

$$R_{ij} = R^\phi_{ij} + \tilde{R}_{ij}, \tag{2.11}$$

where R^ϕ_{ij} is given by

$$R^\phi_{ij} = -2\tilde{D}_i\tilde{D}_j\phi - 2\tilde{\gamma}_{ij}\tilde{D}^k\tilde{D}_k\phi + 4\tilde{D}_i\phi\tilde{D}_j\phi$$
$$- 4\tilde{\gamma}_{ij}\tilde{D}^k\phi\tilde{D}_k\phi, \tag{2.12}$$

where $\tilde{D}_i$ is the covariant derivative with respect to the conformal metric $\tilde{\gamma}_{ij}$. The conformal Ricci tensor, $\tilde{R}_{ij}$, is expressed as

$$\tilde{R}_{ij} = -\frac{1}{2}\tilde{\gamma}^{mn}\partial_{mn}\tilde{\gamma}_{ij} + \tilde{\gamma}_{k(i}\partial_{j)}\tilde{\Gamma}^k + \tilde{\Gamma}^k\tilde{\Gamma}_{(ij)k}$$
$$+ \tilde{\gamma}^{mn}(2\tilde{\Gamma}^k_{m(i}\tilde{\Gamma}_{j)kn} + \tilde{\Gamma}^k_{in}\tilde{\Gamma}_{kmj}). \tag{2.13}$$

During the evolution we also enforce the constraints $\text{Tr}(\tilde{A}_{ij}) = 0$ and $\det(\tilde{\gamma}_{ij}) = 1$ at every time step by using the following substitutions

$$\tilde{A}_{ij} \rightarrow \tilde{A}_{ij} - \frac{\text{Tr}(\tilde{A}_{ij})}{3}\tilde{\gamma}_{ij}, \tag{2.14}$$

$$\tilde{\gamma}_{ij} \rightarrow \tilde{\gamma}_{ij}/\tilde{\gamma}^{1/3}. \tag{2.15}$$

The matter source terms, E, S_i, and S_{ij} appearing in the Einstein equations are projections of the stress-energy tensor $T^{\mu\nu}$ on the hypersurface with respect to the unit normal n^μ

$$E = n_\mu n_\nu T^{\mu\nu}, \quad S_i = -\gamma_{i\mu}n_\nu T^{\mu\nu}, \quad S_{ij} = \gamma_{i\mu}\gamma_{j\nu}T^{\mu\nu}, \tag{2.16}$$

with $S = S_{ij}\gamma^{ij}$.

In addition to the evolution equations there are three constraint equations, the Hamiltonian, the momentum and the Gamma constraints, which are only used as diagnostics of the accuracy of the numerical evolutions

$$\mathcal{H} \equiv \tilde{\gamma}^{ij}\tilde{D}_i\tilde{D}_j e^\phi - \frac{e^\phi}{8}\tilde{R} + \frac{e^{5\phi}}{8}\tilde{A}_{ij}\tilde{A}^{ij} - \frac{e^{5\phi}}{12}K^2$$
$$+ 2\pi e^{5\phi}E = 0, \tag{2.17}$$

$$\mathcal{M}^i \equiv \tilde{D}_j(e^{6\phi}\tilde{A}^{ij}) - \frac{2}{3}e^{6\phi}\tilde{D}^i K - 8\pi e^{6\phi}\tilde{\gamma}^{ij}S_j = 0, \tag{2.18}$$

$$\mathcal{G}^i \equiv \tilde{\Gamma}^i + \partial_j\tilde{\gamma}^{ij} = 0. \tag{2.19}$$

2. Puncture approach

Recent breakthroughs in numerical relativity have finally made possible accurate and long-term stable $3 + 1$ evolutions of singular spacetimes, including the challenging cases of the collision of compact binaries formed by either two BHs or a BH and a NS (see [27] and references therein). One of the key ingredients for such success has been the so-called "puncture approach" [40], in which BH initial data are modeled by the Brill-Lindquist topology [41], where a "throat" at the BH horizon connects two asymptotically flat regions. One of the asymptotically flat ends is compactified to a single point known as the puncture, leading to a coordinate singularity.

The puncture approach has the advantage that its numerical implementation within the BSSN formalism is rather simple. The original proposal only considered the *fixed* puncture approach [39,42,43], where the conformal factor is split into a regular part and a singular part. Although this method does not lead to long-term stable evolutions of spacetimes containing BHs, it allows for a number of code tests. However, two different groups [25,26] developed recently the *moving* puncture approach in which no singular term of the conformal factor is factored out, and the punctures are allowed to move through the grid. The difference between these two methods is how the conformal factor is evolved. In the so-called ϕ-method [26], the original BSSN variable ϕ is evolved through the usual BSSN evolution Eq. (2.5). On the other hand, the so-called χ-method [25] introduces a new conformal factor defined as $\chi \equiv e^{-4\phi}$, and the following evolution equation, that replaces Eq. (2.5),

$$(\partial_t - \mathcal{L}_\beta)\chi = \frac{2}{3}\chi(\alpha K - \partial_j\beta^j). \tag{2.20}$$

This moving puncture approach, together with the so-called puncture gauge (see Sec. II A 3), has led to major success in simulations of binary BHs [44–50]. Motivated by this, we have implemented both methods in our 2D code, the ϕ-method and the χ-method, for the moving puncture approach to investigate the dynamics of matter around BHs.

3. Gauge choices

In addition to the BSSN spacetime variables ($\tilde{\gamma}_{ij}$, $\tilde{A}_{ij}$, K, ϕ or χ, $\tilde{\Gamma}^i$), there are two more variables left undetermined, the lapse, α and the shift vector, β^i. The code can handle arbitrary gauge conditions, however long-term BH evolutions in the moving puncture framework have been suc-

cessful with some combination of the so-called "1 + log" condition [51] for the lapse, and the "Gamma-freezing" condition for the shift vector [39].

The form of this slicing condition most commonly used for moving puncture evolutions contains the advective term $\beta^i \partial_i \alpha$ and is expressed as

$$\partial_t \alpha - \beta^i \partial_i \alpha = -2\alpha K. \qquad (2.21)$$

Several authors (see, e.g. [28,52,53]) have used the so-called "nonadvective 1 + log", by dropping the advective term in Eq. (2.21), for single BH evolutions. In this case, the slicing condition takes the form

$$\partial_t \alpha = -2\alpha K. \qquad (2.22)$$

It was shown by [52], that the evolution of a single puncture using the condition given by Eq. (2.22) settles down into a time-independent and maximally sliced solution.

For the simulations of a BH surrounded by a self-gravitating torus presented in this paper, we choose the slicing given by Eq. (2.22) as the BH does not move through the grid, and therefore the advective term $\beta^i \partial_i \alpha$ does not play an important role.

For the shift vector, we choose the Gamma-freezing condition, written as

$$\partial_t \beta^i = \frac{3}{4} B^i, \qquad (2.23)$$

$$\partial_t B^i = \partial_t \tilde{\Gamma}^i - \eta B^i, \qquad (2.24)$$

where η is a constant that acts as a damping term, introduced both to prevent long-term drift of the metric functions and to prevent oscillations of the shift vector [39]. This parameter also has an effect on the coordinates of the final spacelike hypersurface. In Ref. [53] it was shown that increasing the value of η increases the coordinate size of the BH, which allows for better numerical resolution across the BH. On the other hand, larger values of the damping parameter introduce a higher drift in the location of the horizon in time, as well as in the deformation of the metric during the evolution, caused by the larger values reached by the connection functions $\tilde{\Gamma}^i$ [28,54]. Bearing this in mind, we use $\eta = 0.3/M$, where M is the ADM mass of the system, for the evolutions of spacetimes containing a BH presented in this paper.

B. Formulation of the hydrodynamics equations

The general relativistic hydrodynamics equations, expressed through the conservation equations for the stress-energy tensor $T^{\mu\nu}$ and the continuity equation are

$$\nabla_\mu T^{\mu\nu} = 0, \qquad \nabla_\mu (\rho u^\mu) = 0, \qquad (2.25)$$

where ρ is the rest-mass density, u^μ is the fluid four-velocity and ∇ is the covariant derivative with respect to the spacetime metric. Following [37] the general relativistic hydrodynamic equations are written in a conservative

form in cylindrical coordinates. Since the Einstein equations are solved only in the $y = 0$ plane with Cartesian coordinates, the hydrodynamic equations are rewritten in the Cartesian coordinates for $y = 0$. The following definitions for the hydrodynamical variables are used

$$\rho_* \equiv \rho W e^{6\phi}, \qquad (2.26)$$

$$v^i \equiv \frac{u^i}{u^t} = -\beta^i + \alpha \gamma^{ij} \frac{\hat{u}_j}{hW}, \qquad (2.27)$$

$$\hat{u}_i \equiv h u_i, \qquad (2.28)$$

$$\hat{e} \equiv \frac{e^{6\phi}}{\rho_*} T_{\mu\nu} n^\mu n^\nu = hW - \frac{P}{\rho W}, \qquad (2.29)$$

$$W \equiv \alpha u^t, \qquad (2.30)$$

where W and h are the Lorentz factor and the specific fluid enthalpy, respectively, and P is the pressure.

By defining the vector of unknowns, $\mathbf{U}$, and fluxes $\mathbf{F}^x$ and $\mathbf{F}^z$ along the x and z directions as

$$\mathbf{U} = (\rho_*, J_x, J_y, J_z, E_*), \qquad (2.31)$$

$$\mathbf{F}^x = [\rho_* v^x, J_x v^x + P\alpha\sqrt{\gamma}, J_y v^x, J_z v^x, E_* v^x \\ + P\alpha\sqrt{\gamma}(v^x + \beta^x)], \qquad (2.32)$$

$$\mathbf{F}^z = [\rho_* v^z, J_x v^z, J_y v^z, J_z v^z + P\alpha\sqrt{\gamma}, E_* v^z \\ + P\alpha\sqrt{\gamma}(v^z + \beta^z)], \qquad (2.33)$$

with $J_i \equiv \rho_* \hat{u}_i$ and $E_* \equiv \rho_* \hat{e}$, the set of hydrodynamic Eqs. (2.25) can be written in conservative form as

$$\partial_t \mathbf{U} + \partial_x \mathbf{F}^x + \partial_z \mathbf{F}^z = \mathbf{S}, \qquad (2.34)$$

where $\mathbf{S}$ is the vector of sources. We refer to [37] for further details on these equations, in particular, regarding the form of the source terms.

To close the system of equations, we choose two possible equations of state, the so-called Γ-law equation of state (ideal fluid) given by

$$P = (\Gamma - 1)\rho\epsilon, \qquad (2.35)$$

where ϵ is the specific internal energy, and a polytropic equation of state

$$P = \kappa\rho^\Gamma. \qquad (2.36)$$

Here κ is the polytropic constant, $\Gamma = 1 + 1/N$ and N is the polytropic index. In those simulations where the system evolves adiabatically, such that no shocks are present, we use the polytropic equation of state during the evolution.

After each time iteration the conserved variables (i.e. ρ_*, J_x, J_y, J_z, E_*) are updated and the *primitive* hydrodynamical variables (i.e. ρ, v^x, v^y, v^z, ϵ) have to be recovered at the corresponding step. This is done by solving the follow-

ing equation for the Lorentz factor, W, derived from the normalization of the 4-velocity of the fluid

$$W^2 = 1 + \gamma^{ij}u_i u_j = 1 + \gamma^{ij}\hat{u}_i\hat{u}_j\left(\frac{\hat{e}}{W} + \frac{P}{\rho W^2}\right)^{-2}. \quad (2.37)$$

Once solved for W, the other variables, ρ, v^i, P, ϵ and h are computed from Eqs. (2.26), (2.27), (2.28), (2.29), and (2.30) and the equation of state.

III. NUMERICS

There are two schemes implemented for the update of the numerical solution with time: an iterative Crank-Nicholson (ICN) scheme taking two corrector steps [55], and an optimal strong stability-preserving (SSP) Runge-Kutta of fourth-order algorithm with 5 stages [56] (RK4). The RK4 scheme is used for simulations of spacetimes containing a singularity, where a high-order of accuracy is an important issue.

We use second-order slope limiter reconstruction schemes (both minmod and MC are implemented in the code) to obtain the left and right states of the primitive variables (i.e. ρ, v^x, v^y, v^z, ϵ) at each cell interface, and these reconstructed variables are then used to compute the left and right states of the evolved quantities (ρ_*, J_x, J_y, J_z, E_*). Next, we use HLLE or Roe approximate solvers to compute the numerical fluxes in the x and z directions. Details on such high-resolution shock-capturing schemes are available elsewhere (see e.g. [22] and references therein).

Derivative terms in the spacetime evolution equations are represented by second or fourth-order centered finite difference approximation [57] in a uniform Cartesian grid except for the advection terms (terms formally like $\beta^i \partial_i u$), for which an upwind scheme is used.

A. Discretization of axisymmetric systems: "cartoon" method

As pointed out by [38] any given system of equations in 3D possessing a rotation symmetry with respect to the z-axis can be finite differenced and solved in the $x - z$ ($y = 0$) plane alone because of the symmetry condition. When the system of equations is expressed in Cartesian coordinates, partial derivative terms with respect to the y-coordinate will appear and these need to be computed using the computational domain. For instance, in a second-order centered difference approximation, the values of the derivative in the y-direction of a quantity $f(x, 0, z)$, are computed using the values of f at the nearest two grid points i.e. $f(x, -\Delta y, z)$, $f(x, \Delta y, z)$. Then, because of axisymmetry, the y-derivatives can be determined in the $x - z$ plane from information contained in this same plane. The Cartoon method obtains the boundary conditions at $y = \pm\Delta y$ that are necessary to evaluate the derivatives in the

y-direction by means of a rotation about the symmetry axis of the different tensor quantities. On the other hand, in a fourth-order centered difference approximation, the values of the derivative in the y-direction of a quantity $f(x, 0, z)$, are computed using the values of f at the grid points $f(x, \pm 2\Delta y, z)$ and $f(x, \pm\Delta y, z)$.

The values of the variables at the positions $(\sqrt{x^2 + \Delta y^2}, 0, z)$ and $(\sqrt{x^2 + 4\Delta y^2}, 0, z)$ are interpolated from the neighboring grid points using Lagrange polynomial interpolation (see e.g. [58]) with interpolating polynomials of degree 2 and 4, depending on the order of the finite difference approximation.

B. Boundary conditions

The computational domain is defined as $0 \leq x \leq L$ and $0 \leq z \leq L$, where L refers to the location of the outer boundaries. For simulations with the puncture method we used a staggered Cartesian grid to avoid that the location of the puncture at the origin coincides with a grid point. A number of different boundary conditions are implemented in the code. These are imposed for the spacetime variables or the hydrodynamical primitive variables at the inner and outer boundaries as follows: for both the spacetime and hydrodynamical variables, π-rotation symmetry is imposed around the z-axis, and equatorial plane symmetry with respect to the $z = 0$ plane. At the outer boundaries we impose radiative boundary conditions [39]. Note that we do not apply this boundary condition to the conformal connection functions, $\tilde{\Gamma}^i$, for which we used static boundary conditions.

C. Atmosphere treatment

An important ingredient in numerical simulations based on finite difference schemes to solve the hydrodynamic equations is the treatment of vacuum regions. The standard approach is to add an atmosphere of very low density filling these regions [59]. We follow this approach and treat the atmosphere as a perfect fluid with a rest-mass density several orders of magnitude smaller than that of the bulk matter. The hydrodynamic equations are solved in the atmosphere region in the same way that is done for the region of the bulk matter. If the conservative variables ρ_* or E_* fall below some minimum value then the values of the conserved quantities are set to the atmosphere value. Similarly in the routine that recovers the primitive variables from the conserved variables, if the rest-mass density ρ or specific internal energy ϵ fall in a given grid point below the value set for the atmosphere, such point is reset to have the atmosphere value of the primitive variables. In particular for simulations of relativistic stars, and systems composed of a BH plus a self-gravitating torus system, the atmosphere density is usually taken to be about 6–8 orders of magnitude smaller than the initial maximum rest-mass density.

D. Diagnostics

To check the accuracy of the numerical simulations we monitor the violation of the Hamiltonian constraint, and the conservation of the total rest-mass M_*, the ADM mass M, and the angular momentum J. We compute these various quantities in the $y = 0$ plane as

$$M_* = 4\pi \int_0^L x dx \int_0^L \rho_* dz, \qquad (3.1)$$

$$M = -2 \int_0^L x dx \int_0^L dz \left[-2\pi E e^{5\phi} + \frac{e^\phi}{8} \tilde{R} \right.$$
$$\left. - \frac{e^{5\phi}}{8} \left(\tilde{A}_{ij} \tilde{A}^{ij} - \frac{2}{3} K^2 \right) \right], \qquad (3.2)$$

$$J = 4\pi \int_0^L x^2 dx \int_0^L \rho_* \tilde{u}_y dz. \qquad (3.3)$$

In axisymmetry the apparent horizon (AH hereafter) equation becomes a nonlinear ordinary differential equation (ODE) for the AH shape function, $h = h(\theta)$ [60,61]. We have implemented an AH finder that solves this ODE by a shooting method using that $\partial_\theta h(\theta = 0) = 0$ and $\partial_\theta h(\theta = \pi/2) = 0$ as boundary conditions. We define the mass of the AH as

$$M_{\text{AH}} = \sqrt{\frac{\mathcal{A}}{16\pi}}, \qquad (3.4)$$

where $\mathcal{A}$ is the area of the AH.

IV. VACUUM TESTS: SINGLE BH EVOLUTIONS

The Schwarzschild metric in isotropic coordinates is used as initial data to test the ability of the code to evolve BH spacetimes within the fixed and moving puncture approaches. These initial data are such that the 3-metric is written in Cartesian coordinates as

$$d\sigma^2 = \psi^4(dx^2 + dy^2 + dz^2), \qquad (4.1)$$

where the conformal factor is $\psi = (1 + M/2r)$, M being the mass of the BH. Here r is the isotropic radius, $r^2 = x^2 + y^2 + z^2$. Thus, the spatial metric takes the form $\gamma_{ij} = \psi^4 \tilde{\gamma}_{ij}$, where the conformal metric is the flat metric. Initially the extrinsic curvature is $K_{ij} = 0$.

A. Schwarzschild BH with geodesic slicing

Following the fixed puncture approach, we first evolve these initial data with geodesic slicing, that is setting $\alpha = 1$ and $\beta^i = 0$. Although, in these coordinates, the numerical evolution is known to last very short time and is expected to crash at $t = \pi M$ when the spacelike hypersurface reaches the physical singularity, there is an analytic solution for the evolution of the spacetime which can be used to compare to the numerical solution.

The top-left panel in Fig. 1 shows the evolution of the radial metric component $\tilde{\gamma}_{rr}$, that is obtained from the Cartesian metric functions, along the diagonal for different resolutions together with the analytic solution at several time steps, performed with second-order finite differences in space. The convergence of the code can already be seen in this panel, but this is better appreciated in the bottom-left panel, in which the Hamiltonian constraint is plotted at $t = 2M$ for the three different resolutions. Violations of the Hamiltonian constraint are a measure of the numerical error, and this figure shows that this error scales at the expected rate for second-order convergence. Results obtained with a fourth-order finite differencing are shown in the upper and lower-right panels, where the same quantities are plotted using this higher order differencing. Clearly, using fourth-order finite differencing increases the accuracy of the numerical evolutions, although the convergence rate for the highest resolution is not exactly fourth-order in the whole computational domain. We note that in addition to the numerical error due to the finite difference approximations for the spatial derivatives, there is another source of numerical error due to the interpolation needed with the Cartoon method.

B. Schwarzschild BH with $1 + \log$ slicing

Next, we use a zero shift and a modified $1 + \log$ slicing condition that permits the increase of the life of the simulation up to about 30–40M. The slicing condition used for this simulation is [62],

$$\partial_t \alpha = -2\alpha \psi^4 K. \qquad (4.2)$$

Figure 2 displays the time evolution of one of the components of the conformal three metric and the lapse function, and it proves how the new gauge condition enables for longer simulations. For this simulation we consider a grid resolution of $\Delta x = 0.05M$ with $N_x \times N_z = 200 \times 200$ grid points. As expected, the metric function $\tilde{\gamma}_{xx}$ grows due to the grid stretching related to the collapse of the lapse. In order to increase further the length of the simulations of a single BH spacetime, we have implemented the moving puncture method, and its test is shown next.

C. Schwarzschild BH and the moving puncture approach

It has been pointed out [52,53,63], that using the "moving puncture method" the numerical slices of a Schwarzschild BH spacetime reach a stationary state after about 40M of evolution. [52] computed numerically this time-independent puncture data for the Schwarzschild spacetime and showed that, as the evolution proceeds, the initial slice settles down to a maximal slice with $K = 0$. This time-independent data has recently been obtained analytically by Baumgarte and Naculich [64].
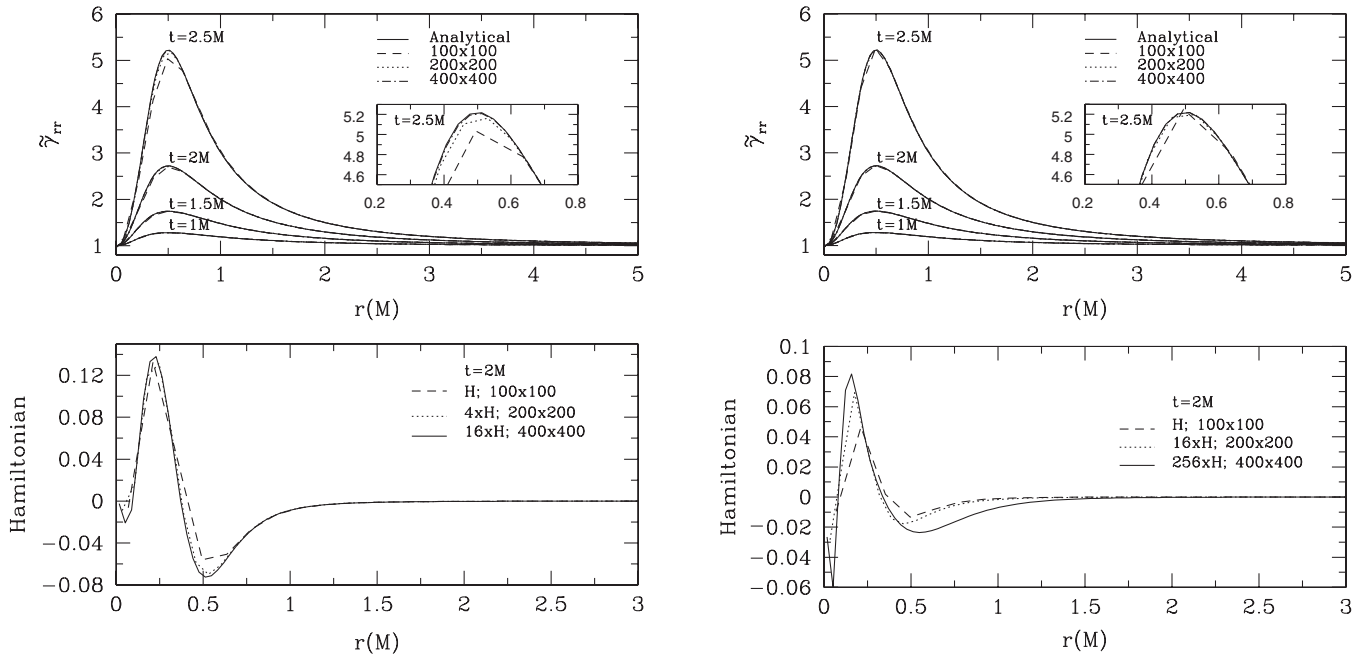
FIG. 1.   Top-left panel: evolution of the conformal metric component $\tilde{\gamma}_{rr}$ along the diagonal of the grid. Different lines refer to the numerical solution with resolutions of 100, 200, and 400 grid points in each direction. The analytical solution is also shown. Bottom-left panel: Hamiltonian constraints along the diagonal at time $t = 2M$ for three different resolutions showing the expected second-order convergence. The right panels show the same quantities and the expected convergence rate when using fourth-order finite differencing.

With the aim of testing the ability of our code to perform long-term, stable and accurate, evolutions of a single BH, we first check the evolution of the BH puncture analytical
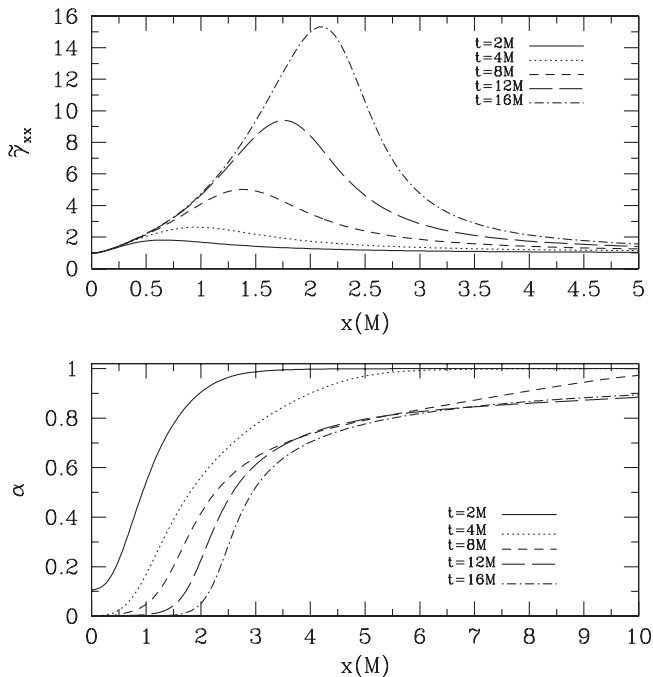
FIG. 2.   Time evolution of the conformal metric component $\tilde{\gamma}_{xx}$ and the lapse α along the x-axis using $1 + \log$ slicing.

data given by [64], with the gauge conditions given by Eqs. (2.22), (2.23), and (2.24), and with two different methods for the evolution of the conformal factor, the ϕ-method, which uses Eq. (2.5), and the χ-method which, instead uses the evolution Eq. (2.20). For the damping parameter in the evolution equation for the shift, we set $\eta = 0.3/M$.

In the upper panel of Fig. 3, we plot the absolute deviations for the conformal factor between our numerical solution and the exact solution at $t = 9M$ obtained with the ϕ-method, for three runs with different resolutions ($\Delta x = 0.12M, 0.06M, 0.03M$, with $N_x \times N_z = 150 \times 150, 300 \times 300, 600 \times 600$). Deviations for the conformal factor are shown in the inner region of the grid, which at $t = 9M$ is not affected by the outer boundary conditions. The inset, shows these deviations from the exact solution, but re-scaled assuming fourth-order convergence. We note approximate fourth-order convergence for the two lower resolutions runs ($\Delta x = 0.12M, 0.06M$), but, although still converging, the convergence rate decreases from fourth-order for the highest resolution run ($\Delta x = 0.03M$) particularly in the region outside the AH. For this resolution the error between the numerical and the analytical solution in the region outside the AH is of the order of 10^{-5}–10^{-6}, and we find that increasing further the resolution does not reduce significantly this error.

In the bottom panel of Fig. 3 we plot again the deviations for the conformal factor, however these are now computed
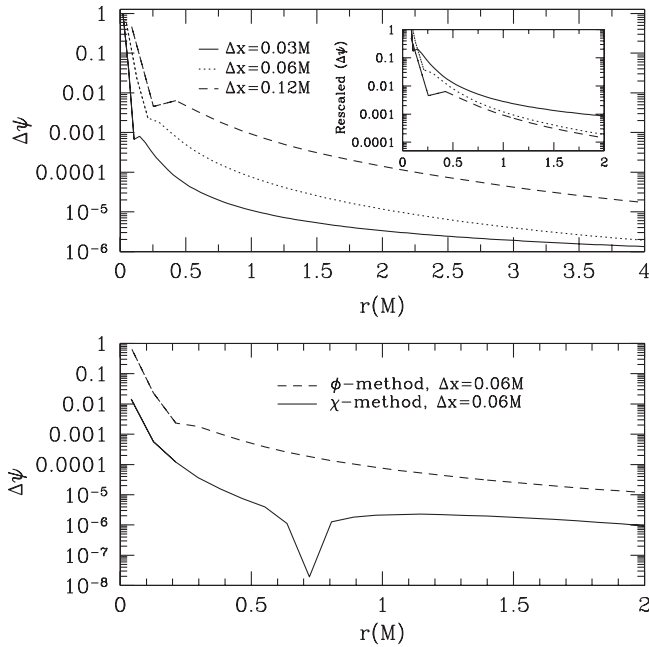
FIG. 3. In the top panel we consider as initial data the analytical solution proposed by Baumgarte and Naculich [64] and show the deviations for the conformal factor from the exact solution for different resolutions using the ϕ-method. In the inset, we show deviations rescaled to show the convergence. In the bottom panel, we show the deviations of the conformal factor using the same resolution, $\Delta x = 0.06M$, with the ϕ-method as well as the χ-method.
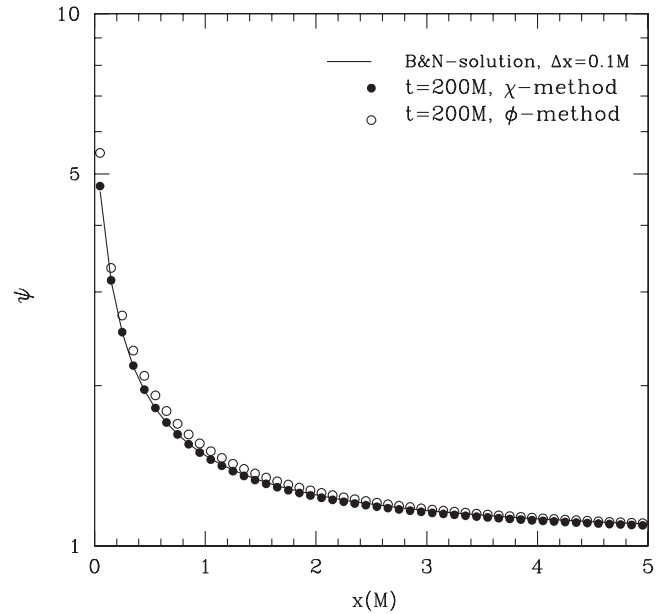

FIG. 4. We show, with a solid line, the conformal factor given by Baumgarte and Naculich [64], and with solid circles the numerical solution for the conformal factor at $t = 200M$ of Schwarzschild spacetime in isotropic coordinates initial data with the χ-method and with empty circles the same quantity but computed using the ϕ-method.

using the χ-method as well as the ϕ-method, and obtained with the same resolution, $\Delta x = 0.06M$, at $t = 9M$. Clearly, the deviations from the exact solution obtained with the χ-method are smaller than with the ϕ-method. In fact, these results are to be expected, as ϕ diverges like log r near the puncture, while χ behaves like r^2 near the puncture.

We next perform a comparison between the time-independent analytical data [64] and the late time numerical solution of a Schwarzschild spacetime time, in isotropic coordinates, choosing initially $\alpha = \psi^{-2}$. For this comparison we use the same gauge conditions as above, grid spacing $\Delta x = \Delta z = 0.1M$ and a grid with $N_x \times N_z = 300 \times 300$ points to cover the computational domain. In Fig. 4, we plot with a solid line the time-independent analytical solution for the conformal factor, while solid circles indicate the numerical solution for the conformal factor of the Schwarzschild spacetime initial data at $t = 200M$, computed using the χ-method and empty circles correspond to the same quantity but using the ϕ-method. Both simulations are compared at a sufficiently late time to allow us to evaluate the effect of the outer boundary conditions on the late time evolution. Clearly, the numerical solution agrees well with the analytical solution, both for the χ and ϕ methods. However, again the χ-method gives better results in the region near the puncture. In addition, we observe that the outer boundary

conditions do not affect the long-term stability and accuracy of these simulations.

V. HYDRODYNAMIC TESTS

A. Relativistic shock-tube test

As a first test of the solution of the relativistic hydrodynamic equations we perform a standard one dimensional shock-tube problem (a Riemann problem) in flat spacetime. This is a common test to assess hydrodynamical codes (see e.g. [65]). In this test, two uniform and different fluid states are initially separated by an interface which is then instantaneously removed. The initial data for the left state is $P_L = 13.33$, $\rho_L = 10.00$, $v_L = 0.00$ and for the right state $P_R = 0.66 \times 10^{-6}$, $\rho_R = 1.00$, $v_R = 0.00$, with the initial interface located at $z = 0.5$. The fluid is assumed to be an ideal fluid with $\Gamma = 5/3$.

The results of the numerical evolution are shown in the left panels of Fig. 5, where we plot the profiles at time $t = 0.3$ of the pressure, density and z-component of the fluid velocity for a shock-tube test along the z-direction. The solid line represents the exact solution of the shock-tube problem computed using the public domain code RIEMANN developed by J. M. Martí and E. Müller [66]. The numerical solution is represented by crosses. We use 400 grid points in the z-direction and a grid spacing of $\Delta z = 1/400$. The particular combination of schemes used for this hydrodynamical test comprise the Roe solver, MC cell-reconstruction, and ICN for the time update.
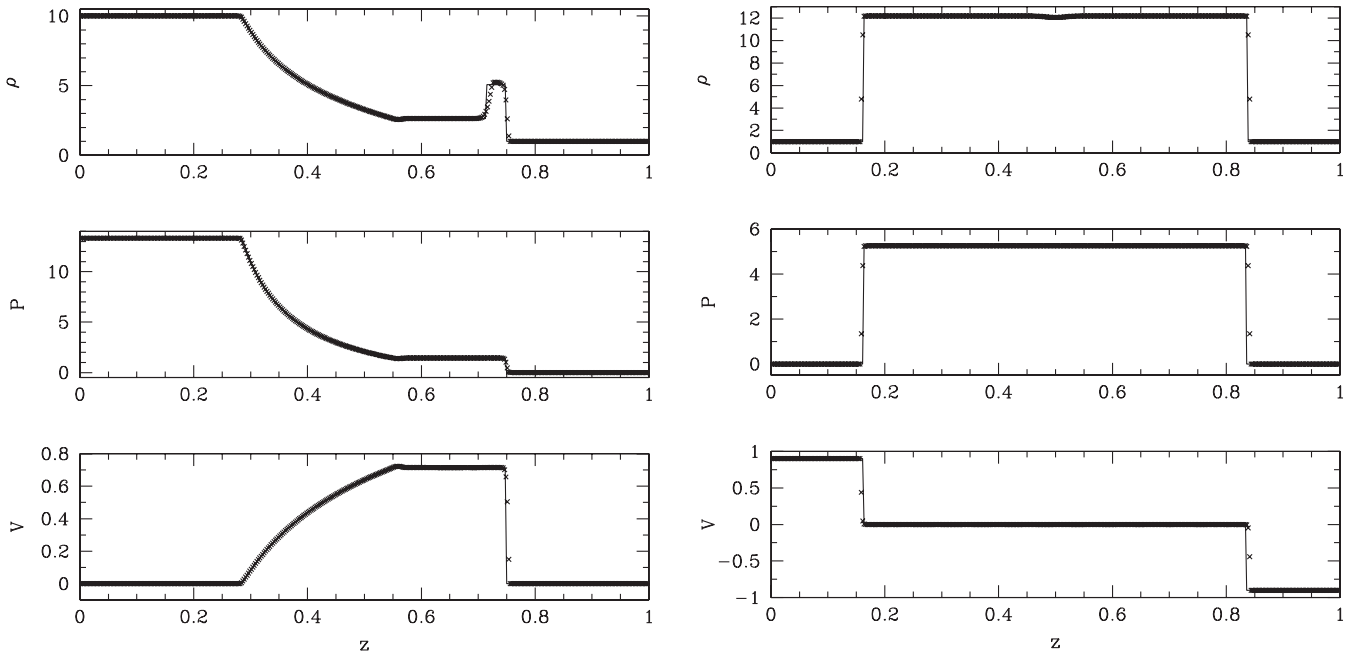
FIG. 5.   Left panel: comparison of the numerical profiles of density, pressure and velocity with the analytical solutions for the solution of a one dimensional shock tube problem at time $t = 0.3$. Right panel: wall shock problem with $v = 0.9$ at time $t = 1.6$. The exact solution is represented by the solid line and numerical solution by crosses.

B. Relativistic planar shock reflection test

In our second test in Minkowski spacetime we carry out a relativistic planar shock reflection problem along the z-direction with the following initial conditions $P = 10^{-6}$, $\rho = 1.0$ in the entire domain, while $v = 0.9$ for $z < 0.5$, and $v = -0.9$ for $z > 0.5$. We use an ideal fluid equation of state with $\Gamma = 4/3$. We show results of the evolution in the right panels of Fig. 5, where we plot the profiles of the solution at time $t = 1.6$ for the pressure, density and z-component of the fluid velocity. Again, the solid lines refer to the analytic solution while the numerical solution is represented by crosses. The schemes used for this simulation are the HLLE solver, minmod cell-reconstruction, and ICN for the time update.

C. Relativistic spherical shock reflection test

The initial configuration for this test problem consists of a medium with uniform density ($\rho = 1$) and pressure ($P = 2.29 \times 10^{-5}(\Gamma - 1)$) where $\Gamma = 4/3$, with constant spherical inflow velocity $v_{\rm in} = -0.9$ and Lorentz factor $W_{\rm in}$. Initially, at $t = 0$, the gas collides at the center of symmetry which forms a strong shock wave that propagates upstream. The analytic solution for this test has the following form [67]

$$\rho(r, t) = \begin{cases} (1 + \frac{|v_{\rm in}|t}{r})^2, & r > v_{\rm s}t, \\ (1 + \frac{|v_{\rm in}|}{v_{\rm s}})^2\sigma, & r < v_{\rm s}t, \end{cases} \quad (5.1)$$

with the compression ratio given by

$$\sigma = \frac{\Gamma + 1}{\Gamma - 1} + \frac{\Gamma}{\Gamma - 1}(W_{\rm in} - 1), \quad (5.2)$$

and the shock velocity by

$$v_{\rm s} = \frac{\Gamma - 1}{W_{\rm in} + 1}W_{\rm in}|v_{\rm in}|. \quad (5.3)$$

This test problem has been proposed by [68] to test the ability of a three-dimensional special relativistic hydrodynamics code in Cartesian coordinates to keep the spherical symmetry of the solution. For our axisymmetric hydrodynamics code in Cartesian coordinates, this is a two-dimensional test problem, which allow us to evaluate the solution of the hydrodynamic equations both in the x and z directions. We use $N_x \times N_z = 400 \times 400$ grid points with $\Delta x = \Delta z = 1/400$ to cover the computational domain. The schemes used for this simulation are the HLLE solver, minmod cell-reconstruction, and ICN for the time update.

We show results of the evolution in Fig. 6, where we plot the profiles of the solution at time $t = 3$ for the density, pressure and fluid velocity along the diagonal. The solid line represents the analytic solution while the numerical solution is represented by crosses.

To quantify the error we computed the relative global error between the numerical and the analytical solution defined by $\epsilon_{\rm rel} = \epsilon_{\rm abs}/[\sum_{i,k}|w(x_i, z_k, t_n)|\Delta x\Delta z]$, where the absolute global error is $\epsilon_{\rm abs} = \sum_{i,k}|w_{i,k}^n - w(x_i, z_k, t_n)|\Delta x\Delta z$, $w_{i,k}^n$ is the numerical solution and $w(x_i, z_k, t_n)$ is the analytical solution. We find that the
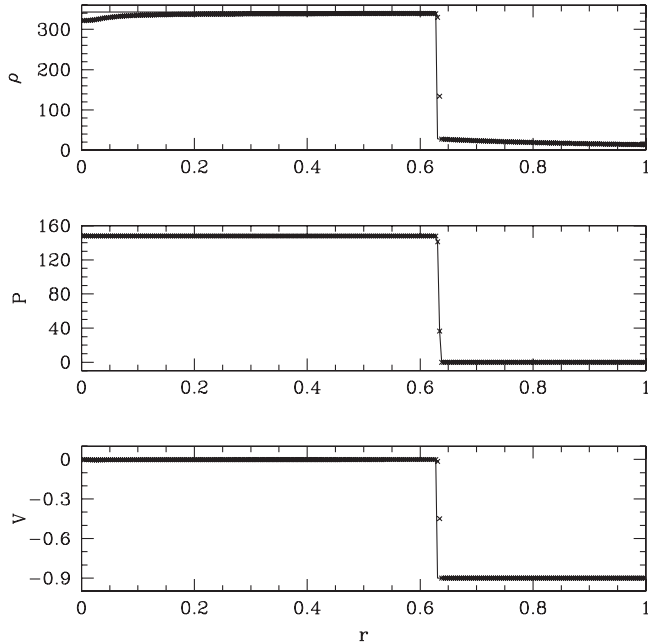
FIG. 6. Comparison of the numerical profiles of density, pressure and velocity with the analytical solutions for the solution of a relativistic spherical shock reflection test at time $t = 3$.

relative global errors for the density, pressure and velocity are 2.1%, 1.1% and 0.6%, respectively. As for the previous shock-tube test and planar shock reflection test, the agreement achieved between the analytic and numerical solution is remarkable.

D. Spherical relativistic stars in a fixed spacetime

For the next test we use the solution of the Tolman-Oppenheimer-Volkoff (TOV) equations to assess the capability of the code to perform long-term stable numerical simulation of a NS in equilibrium. In order to check the hydrodynamical evolution independently from the spacetime evolution we follow the common approach of keeping the spacetime fixed during the numerical evolution. This is known as the Cowling approximation [69], in analogy with the corresponding approximation in perturbative studies of stellar oscillations in which the metric components (or the gravitational potential in the Newtonian framework) are kept constant.

It has been shown [59] that the truncation errors of the finite difference representation of the PDEs are enough to excite small periodic radial oscillations which manifest themselves as periodic variations of the hydrodynamical (and spacetime) quantities. The power spectrum of the evolution of the central density provides the frequencies of the fundamental mode of oscillation and of its overtones, which can be compared with the corresponding frequencies computed by perturbative techniques. Although the excited oscillations are purely numerical in origin (i.e. their amplitude converges to zero as the resolution increases)

they still represent the oscillation modes of the relativistic star and their frequencies should agree with the eigenfrequencies computed by linear perturbation analysis. For the purposes of further testing the code and compare with independent results we focus on an initial TOV model that has been extensively investigated numerically by [59,70]. This model is a relativistic star with $N = 1$, polytropic constant $\kappa = 100$ and central rest-mass density $\rho_c = 1.28 \times 10^{-3}$ so that its mass is $M = 1.4$, its baryon rest-mass $M_* = 1.5$ and its radius $R = 9.59$. We evolve these initial data with our nonlinear code and compute the power spectrum of the evolution of the central rest-mass density. We note that in the simulations of spherical stars in equilibrium presented below, we use the polytropic equation of state during the evolution.

In the upper-left panel of Fig. 7 we plot the time evolution of the central rest-mass density for a simulation with $\Delta x = 0.15$. We observed that the truncation errors at this resolution are enough to excite small periodic radial oscillations, visible in this plot as periodic variations of the central density. We see that the damping of the periodic oscillations of the central rest-mass density is very small during the whole evolution, which highlights the low numerical viscosity of the schemes implemented. By computing the Fourier transform of the time evolution of the central rest-mass density we obtain the power spectrum, which is shown with a solid line in the lower-left panel of the figure, while the dashed vertical lines indicate the fundamental frequency and the first five overtones computed by [70] with a nonlinear hydrodynamics code using spherical polar coordinates. The agreement found for the fundamental frequency and overtones is very good, with the relative error between the fundamental frequencies being less than 1%.

E. Spherical relativistic stars in a dynamical spacetime

For our first test of the coupling of the Einstein equations and the general relativistic hydrodynamic equations we again use the TOV solution. In analogy to what happens in the Cowling approximation, truncation errors excite small oscillations in the star. Now, however, the truncation errors come not only from the hydrodynamic part of the code but also from the spacetime part solving the full set of Einstein equations.

We computed the eigenfrequencies of the coupled evolution of the same TOV star with $\kappa = 100$, $N = 1$ and central rest-mass density $\rho_c = 1.28 \times 10^{-3}$ which has been discussed above under the assumption of a fixed background spacetime. Again, the radial oscillations excited by truncation errors manifest in the time evolution of the central rest-mass density. The coupling to the spacetime increases the amplitude of the oscillations, and also shifts the frequencies of the modes towards lower frequencies. This is shown in the lower-right panel of Fig. 7 which displays the power spectrum of the evolution of the central
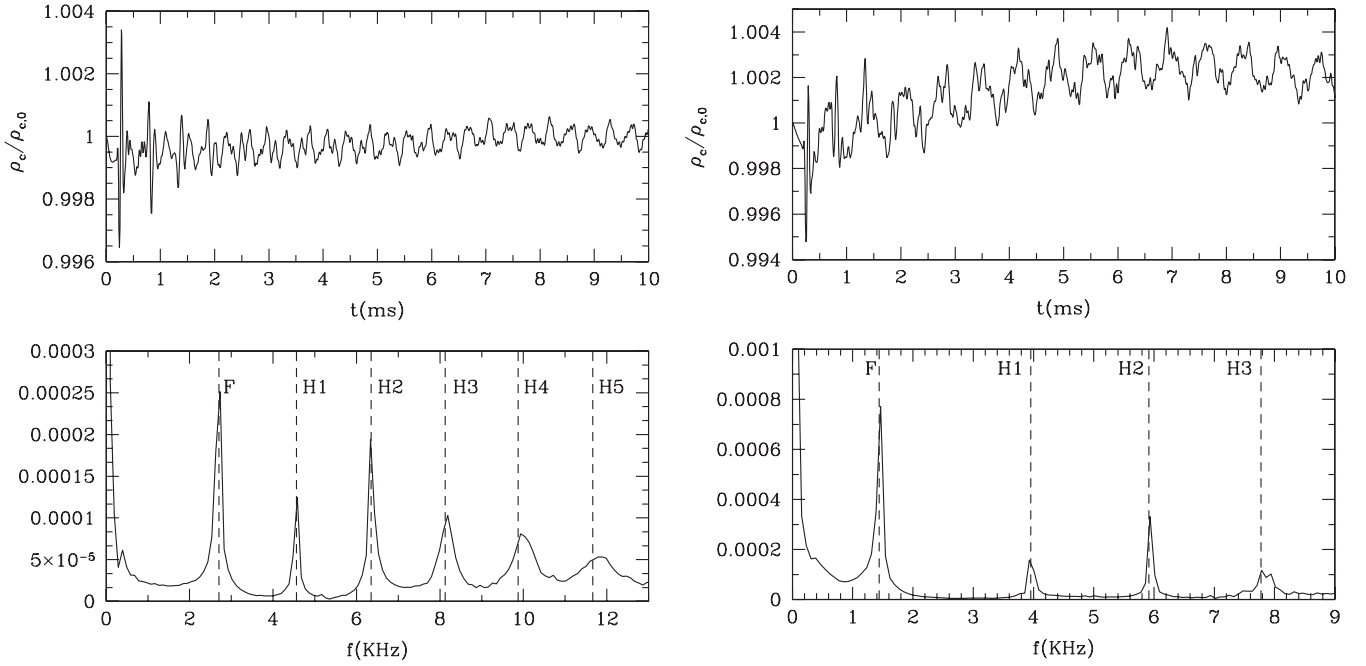
FIG. 7.   Top panels show the time evolution of the normalized central density, in the Cowling approximation (left panel), and in a dynamical spacetime evolution (right panel). Power spectrum of the evolution of the central rest-mass density for an $M = 1.4$, $\kappa = 100$, $N = 1$ polytrope in the Cowling approximation (bottom-left panel). F represents the frequency of the fundamental mode and H1-H6 are the first six overtones computed by [70]. Correspondingly, the bottom-right panel shows the same quantities in a dynamical spacetime evolution of the same TOV star. The frequencies computed by [59] are displayed with dashed vertical lines.

rest-mass density (solid line), and the eigenfrequencies computed by [59] (dashed lines). We note that the locations of the frequency peaks for the fundamental mode and the two overtones is in very good agreement, with the relative error in the fundamental frequencies being less than 1%.

F. Gravitational collapse of marginally stable spherical relativistic stars

We next test the capability of the code to follow BH formation with the gravitational collapse to a BH of a marginally stable spherical relativistic star. For this test, we consider a $\kappa = 100$, $N = 1$ polytropic star with central rest-mass density $\rho_c = 3.15 \times 10^{-3}$, its mass is $M = 1.64$ and its baryon rest-mass $M_* = 1.79$. In order to induce the collapse of the star we initially increase the rest-mass density by 0.5%.

We present numerical results for the simulation of the gravitational collapse of a marginally stable spherical relativistic star performed with $\Delta x = \Delta z = 0.1M, 0.075M, 0.05M$ to show the convergence of the code. With these resolutions the star is initially covered by approximately 60, 80 and 120 points. The hydrodynamics equations are solved using the Roe solver and MC reconstruction, while the Einstein equations are solved with fourth-order finite differencing and the gauge conditions given in Eqs. (2.22), (2.23), and (2.24), with $\eta = 0.5$. Time integration is done with RK4. We plot in Fig. 8 the time evolution of the
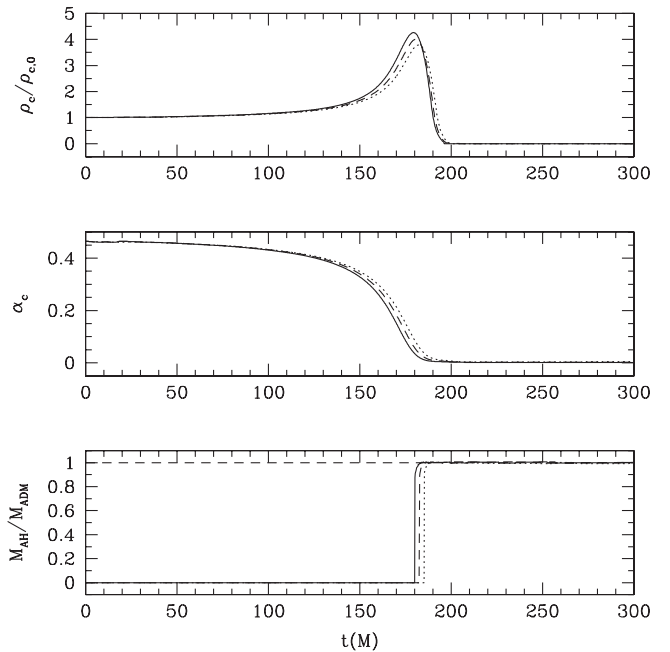

FIG. 8.   Time evolution of the normalized central density, the central lapse function, and mass of the AH in units of the ADM mass of the system for the collapse of a marginally stable spherical star to a BH. Dotted lines represent results obtained with the lowest resolution, dashed lines with the medium resolution while solid lines with the highest resolution.

normalized central density (top panel), of the lapse function at the center (middle panel), and of the mass of the AH (Eq. (3.4)) in units of the ADM mass of the system (bottom panel). Dotted lines represent results obtained with the lowest resolution, dashed lines with the medium resolution while solid lines with the highest resolution. Overall, as the collapse proceeds the star increases its compactness, and is reflected in the increase of the central density as shown in the top panel. The middle panel shows the characteristic collapse of the lapse function at the center of the star indicating the formation of a BH. The most unambiguous signature of the formation of a BH during the simulation is the formation of an AH. Once an AH is found by the AH finder, we monitor the evolution of the AH area, and also of its mass which is plotted, in the bottom panel of Fig. 8. This panel shows that the formation of the BH delays with decreasing resolution, since the increase of the central density slows down because numerical dissipation is larger for the lower resolution runs. An AH is first found at approximately at $t = 180M$ ($t = 0.88$ ms) for the simulation with $\Delta x = \Delta z = 0.05M$. This figure also shows that the mass of the AH relaxes to the ADM mass of the system. The difference in the ADM mass and the mass of the AH when we stop the evolution at $t = 300M$, about $120M$ after the AH is first found, is less than 1%.

This test shows that the code is able to follow BH formation and its subsequent evolution for many timescales. We note that, unlike the results discussed in [29], we do not need to add any numerical dissipation to the evolution equations for the spacetime variables and gauge quantities to perform this simulation. Instead, we rely only on the gauge choice used here to follow the formation and evolution of the BH formed as a result of the gravitational collapse.

G. Rapidly rotating relativistic stars

The evolution of stable rapidly rotating relativistic stars is a more demanding test than all previous ones, as this involves testing parts of the code that are now used since there is a nonzero y-component of the shift vector. The initial data used for this test are the numerical solution of a stationary and axisymmetric equilibrium model of a rapidly and uniformly rotating relativistic star with angular velocity Ω, which has been computed using the `Whisky` code [29,71]. The initial data for this equilibrium rotating star are initially computed in spherical polar coordinates and then transformed to Cartesian coordinates using the standard coordinate transformation.

Here, we consider a uniformly rotating polytropic star with $\Gamma = 2$, $\rho_c = 1.28 \times 10^{-3}$, and rotating at 92% of the allowed mass-shedding limit for a star with the same central rest-mass density. The ratio of the polar to equatorial coordinate radii for this model is 0.7, its mass is $M = 1.57$ and its baryon rest-mass $M_* = 1.69$. For this simulation we use the "$1 + \log$" condition for the lapse, and the
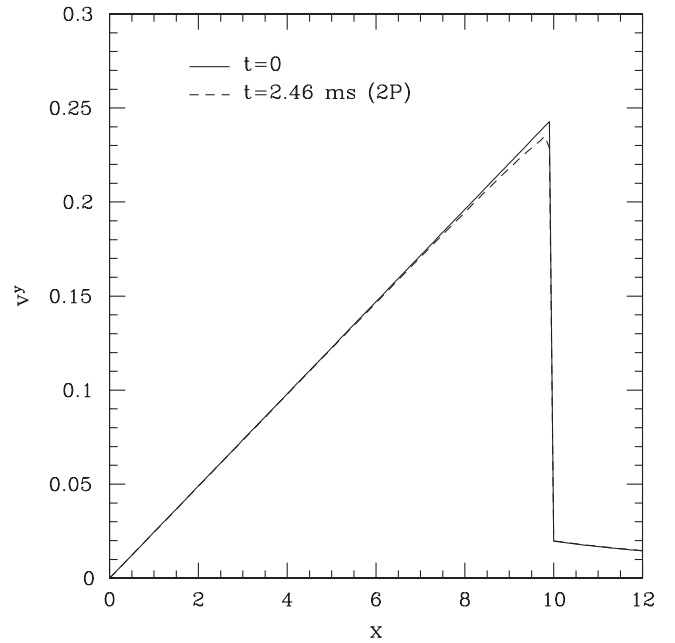

FIG. 9. Profile of the y-component of the velocity of a rapidly rotating relativistic star along the x-axis, at the initial time (solid line) and at time $t = 2.46$ ms, which corresponds to 2 rotational periods.

"Gamma-freezing" condition for the shift vector, with $\eta = 3.0$. We use the so-called Γ-law equation of state during the evolution.

For this test, the outer boundary of the grid is placed about 3 times the equatorial radius. We check that during the evolution, the profiles of the different variables are kept very close to their initial value for several rotational periods, which is shown in Fig. 9. Here we display the profile of the y-component of the velocity, v^y, along the x-axis at the initial time, $t = 0$ (solid line) and at $t = 2.46$ ms (dashed line), with the latter corresponding to two rotational periods. As has been shown by [59,72], the small difference originating at the surface of the star after two rotational periods is expected since we used a second-order reconstruction method with the MC limiter. Nevertheless, it shows that deviations of the numerical solution from the initial profile are very small.

VI. SIMULATIONS OF SELF-GRAVITATING TORUS IN EQUILIBRIUM AROUND A BH

A. Initial data for BH and self-gravitating torus system

The initial data for the numerical simulations of the system formed by a BH and a self-gravitating torus in axisymmetric equilibrium have been recently computed by [30]. The basic equations for the metric functions are derived assuming the $3 + 1$ formalism, and the line element is written in the quasi-isotropic form as

$$ds^2 = -\alpha^2 dt^2 + \psi^4[e^{2q}(dr^2 + r^2 d\theta^2)$$
$$+ r^2\sin^2\theta(\beta dt + d\varphi)^2], \qquad (6.1)$$

where e^{2q} denotes the conformal metric for the rr and $\theta\theta$ parts. The equations for the metric functions are solved in the BH puncture framework, and it is assumed that the puncture is located at the origin.

The equilibrium configurations for the matter are obtained by assuming a perfect fluid stress-energy tensor, and adopting a polytropic equation of state. The only nonzero components of the fluid four-velocity are u^t and u^φ, and initial configurations can be constructed with either constant or nonconstant specific angular momentum distributions, defined as $j \equiv hu_\varphi$. We refer to [30] for a full explanation of the construction of the initial model. For the simulations reported in this paper, we have considered a torus around a Schwarzschild BH (of mass $M_{BH} = 1$). The adiabatic index is $\Gamma = 4/3$ to mimic a degenerate relativistic electron gas, and the polytropic constant κ is fixed to $\kappa = 0.0301262$ such that the torus-to-BH mass ratio, M_t/M_{BH}, is roughly 0.1.

The initial model is computed on a spherical grid. Therefore, in order to use it as initial data for our evolution code, we transform into Cartesian coordinates and interpolate the values of the metric functions and hydrodynamic variables onto a cell-centered Cartesian uniform grid, retaining data for the $y = 0$ plane.

The chosen torus has a constant distribution of specific angular momentum such that its inner and outer edges on the equatorial plane are located at $r_{in} = 7.1M$ and $r_{out} = 14.0M$, where M is ADM mass of system. Thus, such torus is initially covered with approximately 140 points along the x-axis. The center of the torus is defined as the location at which the rest-mass density reaches its maximum and it is located at $r_{max} = 9.8M$. The dynamical timescale, which we choose as the orbital period at the center of the torus, is $t_{orb} = 223M$, that corresponds to about 1.1 ms for the case that $M = M_\odot$.

For these simulations we use an equally spaced uniform grid with a grid spacing $\Delta x = \Delta z = 0.05M$ and a grid with $N_x \times N_z = 600 \times 600$ points to cover a computational domain, $0 \le x \le L$ and $0 \le z \le L$, with $L = 30M$. We use 4th-order finite differencing for the spacetime evolution, and Roe solver with MC reconstruction for the hydrodynamic evolution. The time integration is done with RK4.

B. Dynamics in a fixed spacetime

We have first investigated the equilibrium of the torus by performing numerical evolutions in a fixed spacetime, which nevertheless has the contribution coming from the self-gravity of the torus itself. This permits for one more test of the ability of the code to keep the stationarity of a fluid configuration initially in equilibrium. The accuracy check of the evolution is performed by comparing the stationarity and conservation of different local and global fluid quantities over a timescale which is several times the dynamical one.

We show in Fig. 10 the isocontours of the logarithm of the rest-mass density of the torus as computed at the initial time $t = 0$ (left panel) and at $t = 1100M$ (right panel), the later corresponding to 5 dynamical timescales, when the code was stopped after approximately 3×10^4 iterations, with no sign of the presence of numerical instabilities. These snapshots of the rest-mass density distribution clearly show the stationarity of the initial model for a sufficiently long period of time, and that the morphology of the torus remains unchanged for the duration of the simulation. In addition, they reflect that the treatment of the atmosphere in the vacuum region does not perturb the equilibrium, and does not affect the dynamics during the evolution.

Other quantities that provide a more precise measure of the stationarity of the torus are displayed in Fig. 11, in which we plot the time evolution of three fluid quantities normalized to their initial values. On the top panel, we plot the time evolution of the total rest-mass of the torus,
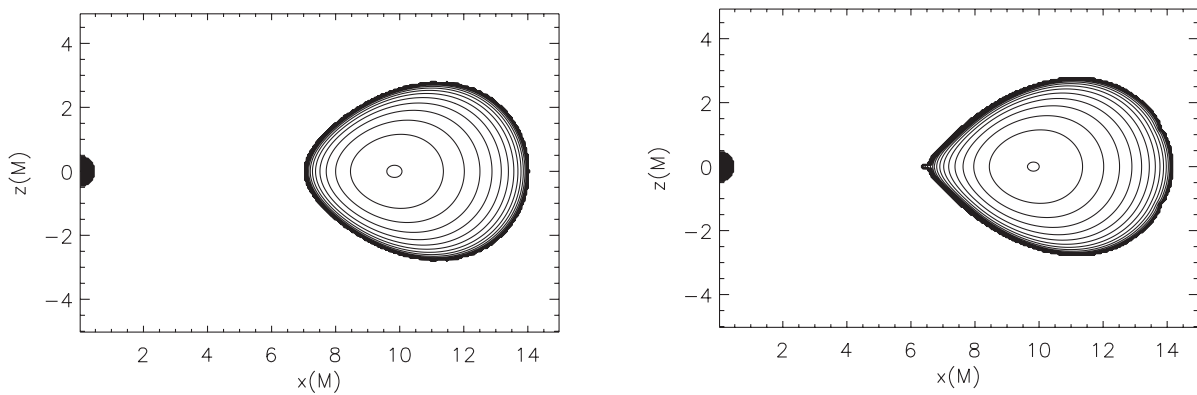

FIG. 10. Isocontours of the logarithm of the rest-mass density of the torus. The left panel shows the configuration at the initial time and the right panel the corresponding distribution after 5 dynamical timescales (approximately 1000M). The equilibrium solution is preserved to high accuracy.
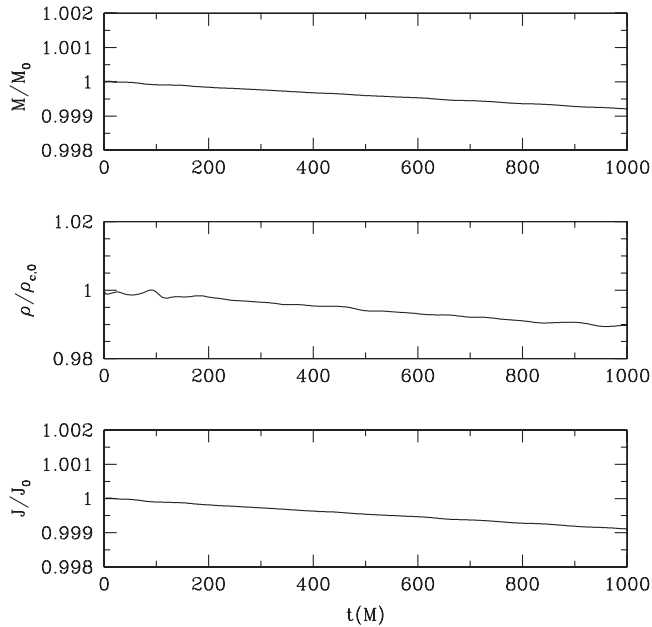
FIG. 11. Time evolution of the total rest-mass, central rest-mass density and total angular momentum, each of them normalized to its initial value, for the evolution of a self-gravitating torus on a fixed spacetime.

normalized to its initial value. At the end of the simulation, the difference between the final total rest-mass with respect to the initial value is less than 10^{-3}. This decrease of 0.1% of the total rest-mass is due to numerical error during the evolution, as the rest-mass is not conserved exactly. However, this error does not affect significantly the stability of the torus for the duration of our simulation. Similar results are obtained for the time evolution of the other two quantities, the central rest-mass density and the total angular momentum, which are displayed in the lower two panels of Fig. 11, respectively. The central rest-mass density, after a short initial transient phase, settles down to a stationary value which only differs after $t = 1000M$ by 1% from the initial one. This provides a strong evidence of the ability of the code to keep the torus in equilibrium for evolutions longer than the characteristic dynamical timescales of these objects.

Notwithstanding the use of Cowling approximation, we can nevertheless extract some information about the oscillating behavior of these type of self-gravitating tori. We note that in a series of recent papers, [73–77], it was shown that upon the introduction of perturbations, non self-gravitating relativistic tori in equilibrium manifest a long-term oscillatory behavior lasting for tens of orbital periods. An important feature of these axisymmetric p-mode oscillations of accretion tori is that the lowest-order eigenfrequencies appear in the harmonic sequence 2:3. Overall, it was found that the 2:3 harmonic sequence was present with a variance of ~10% for tori with a constant distribution of specific angular momentum and

with a variance of ~20% for tori with a power-law distribution of specific angular momentum. The departure from the 2:3 harmonic sequence depends on a number of different elements that contribute to small deviations, such as the vertical size of the tori, the BH spin, the distribution of specific angular momentum, the EOS considered, and the presence of a small but nonzero mass-loss, which can all influence this departure.

In order to trigger the phase of small oscillations of the self-gravitating torus in our simulations, we perturb the equilibrium solution by adding a small perturbation in the x-component of the velocity (we recall that in equilibrium the x and z-components of the velocity are zero). The oscillations reflect in the time evolution of the different fluid quantities, for instance, the central rest-mass density, which we Fourier-transform to obtain the resulting power spectra. This shows distinctive peaks at the frequencies that can be identified with the quasinormal modes of oscillation of the disk. In Fig. 12 we present, in the upper panel, the time evolution of the normalized central rest-mass density of the perturbed model. Because of the initial perturbation, the torus shows a persistent oscillating phase around its equilibrium position. We follow the evolution for about 13 dynamical timescales, and compute the power spectrum obtained from the normalized central rest-mass density, which is shown in the lower panel. A rapid look at this figure reveals that the torus power spectrum shows features which are very similar to those mentioned above for non self-gravitating tori (see e.g. Fig. 4 of [76]). Namely, it can
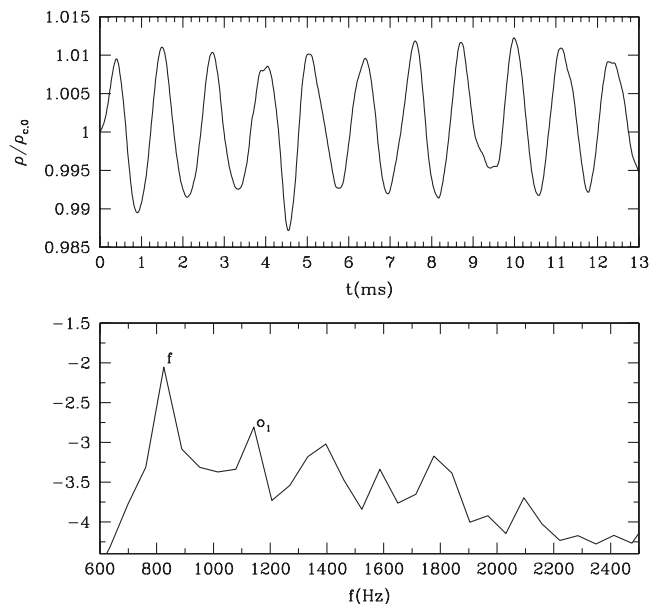

FIG. 12. The upper panel shows the time evolution of the normalized central rest-mass density of a perturbed torus model, while the lower panel displays the power spectrum obtained after Fourier transforming the time evolution of the central rest-mass density. The fundamental mode and first overtone frequencies are denoted by f and o_1. The mass of the BH is taken to be $1M_\odot$.

be clearly identified in the spectrum a fundamental mode f, and a first overtone o_1. Interestingly, the ratio of the fundamental mode and the first overtone also show approximately the 2:3 harmonic relation with $o_1/f \sim 1.4$. In addition, the power spectrum reveals a series of higher frequency peaks, which roughly coincide with linear combinations of the f mode and first overtones. However, simulations lasting for longer timescales are needed to unambiguously identify these peaks.

C. Evolutions on a dynamical spacetime

Next, we evolve the same torus and BH initial data in a fully dynamic way, solving the Einstein equations coupled to the general relativistic hydrodynamics equations. For such simulations we use the gauge conditions given in Eqs. (2.22), (2.23), and (2.24) together with the χ-method, which allow for long-term and stable evolutions of the puncture.

In our simulations of the system formed by a BH plus a self-gravitating torus, the spacetime evolution is highly dynamical until $t \simeq 30M$ due to the initial adjustment of the gauge, which produces a small pulse in the metric functions that propagates outwards. Outgoing radiative boundary conditions for the spacetime variables at the outer boundaries, permit this initial pulse to leave the grid. Despite this initial transient phase, the torus remains in equilibrium during the evolution, and its morphology is kept very close to the initial profile even several hundred M beyond the first orbit when we stopped our simulation. In Fig. 13, we plot the isocontours of the logarithm of the rest-mass density of the torus at time $t = 600M$, which is close to 3 dynamical timescales. This figure clearly demonstrates that the configuration remains in equilibrium. Other quantities also exhibit this behavior. In particular, in Fig. 14, we plot the time evolution of the total rest-mass of the torus (top panel), the central rest-mass density (middle panel), and the total angular momentum (lower panel), each nor-
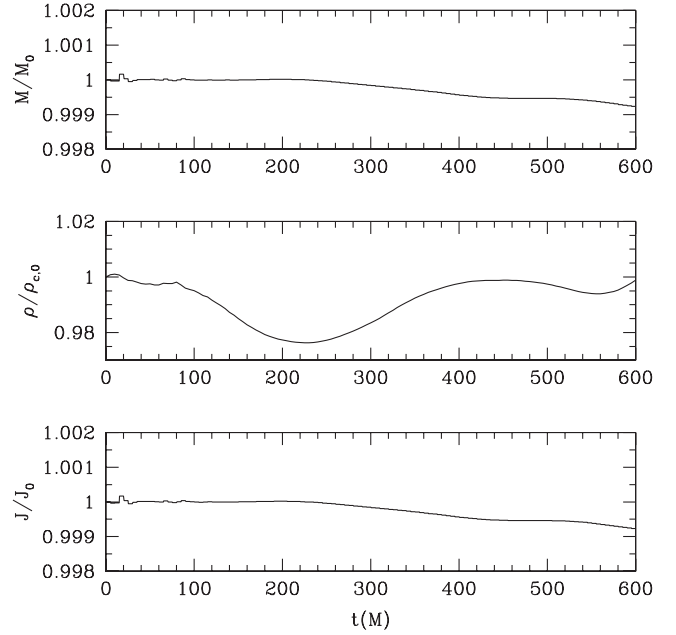
FIG. 14. Time evolution of the total rest-mass density, central rest-mass density and total angular momentum, each of them normalized to its initial value, for the evolution on a dynamical spacetime.

malized to its initial value, for the duration of the simulation. At the end of the simulation, the difference between the final total rest mass with respect to the initial value is less than 0.1%. Although it is due to accumulated numerical error during the evolution, this violation of the rest mass does not affect significantly the stability of the torus for the duration of our simulation. Similar results are obtained for the time evolution of the other two quantities, the central rest-mass density and the total angular momentum. We note that, truncation errors at the resolution employed seem to be enough to trigger small oscillations of the torus around its equilibrium as shown in the evolution of the central rest-mass density.

It is worthwhile to mention, that in order to maintain the torus in equilibrium for several hundred M, we find crucial not to replace the $\tilde{\Gamma}^i$ by $-\partial_j \tilde{\gamma}^{ij}$ on the right-hand side of the evolution Eq. (2.9) whenever is not differentiated. Replacing $\tilde{\Gamma}^i$ by $-\partial_j \tilde{\gamma}^{ij}$ excites larger amplitude oscillations of the torus, which can be more than 10% larger than in the case where $\tilde{\Gamma}^i$ is not replaced by its definition. We note also that, as observed for single puncture simulations in vacuum, numerical errors in the spacetime evolution, especially near the puncture, are smaller with the χ-method than with the ϕ-method. We find that an additional ingredient that helps to maintain the torus equilibrium for the duration of the simulations is the use of the χ-method for the evolution of the conformal factor (we refer to Fig. 3 and 4 for a comparison of the χ-method and ϕ-method). We find numerical indications that, at least in conjunction with the Cartoon method, these two proce-
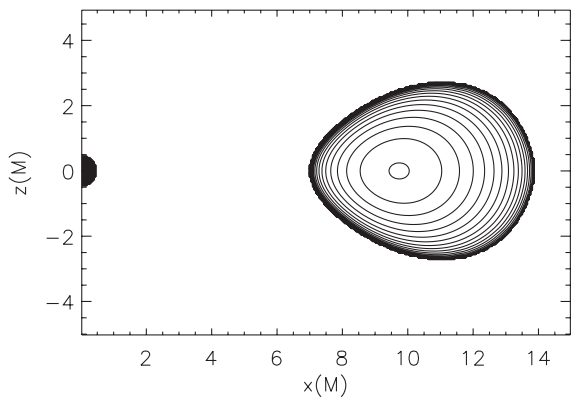

FIG. 13. Isocontours of the logarithm of the rest-mass density of the torus during the evolution on a dynamical spacetime at $t = 600M$. (Compare with the left panel of Fig. 10.)

dures help to decrease the error in the violation of the Hamiltonian constraint.

VII. CONCLUSION

In this paper we have presented a new two-dimensional numerical code designed to solve the full Einstein equations coupled to the general relativistic hydrodynamics equations. The code is mainly intended for studies of self-gravitating accretion disks around BHs, although it is also suitable for regular spacetimes.

Concerning technical aspects, the Einstein equations are formulated and solved in the code using a reformulation of the standard $3 + 1$ (ADM) system, the so-called BSSN approach, in conjunction with the Cartoon method to impose the axisymmetry condition under Cartesian coordinates, and the puncture/moving puncture approach to carry out BH evolutions. We note that a key and novel feature of the code is that combines a fourth-order finite difference approximation for derivative terms in the spacetime evolution with the Cartoon method. Correspondingly, the general relativistic hydrodynamics equations are written in flux-conservative form and solved with high-resolution, shock-capturing schemes.

We have performed and discussed a number of tests to assess the accuracy and expected convergence of the code, namely, (single) BH evolutions, shock tubes, and evolutions of both spherical and rotating relativistic stars. We have also presented a simulation of the gravitational collapse to a BH of a marginally stable spherical star. We have shown that the code is able to handle the formation of a BH, and to follow the BH evolution until we the simulation is stopped after several hundred M. We remark that we did not add any numerical dissipation to the evolution equations for the spacetime variables and gauge quantities to perform this simulation; and exclusively relied on the gauge choice to follow the BH formation and its long-term evolution. Overall, the code has passed those tests with remarkable accuracy.

In addition, paving the way for specific applications of the code, we have also presented results from fully general relativistic numerical simulations of a system formed by a BH surrounded by a self-gravitating torus in equilibrium. First, simulations using a fixed spacetime evolution, have shown that the torus remains in equilibrium around its initial configuration for more than 5 dynamical timescales, when the simulation was stopped. Furthermore, after adding a small perturbation on the torus in equilibrium, we have followed the evolution of the torus through a phase of

small oscillations for more than 13 dynamical timescales. The computation of the frequencies of the fundamental mode of oscillation and the first overtone revealed that these two frequencies appear close to the 2:3 harmonic relation observed for the case of non self-gravitating relativistic tori.

Our simulation of the same model in a dynamical spacetime, showed that the code is able to keep the torus in equilibrium for the several hundred M that lasted the simulation. We have found numerically, that using the χ-method and not to replace the $\tilde{\Gamma}^i$ by $-\partial_j \tilde{\gamma}^{ij}$ on the right-hand side of the evolution for the Γ^i are two important issues that reduce the numerical error in the spacetime evolution, and therefore, help to maintain the torus in equilibrium.

Overall, the simulations performed indicate that the code is able to perform such simulations accurately and for the sufficient duration needed to produce scientific results for one of the specific applications for which it has been designed, the investigation of the runaway instability of thick accretion disks around BHs. We point out that the last simulation presented in the paper is the first 2D axisymmetric simulation of the system formed by self-gravitating torus around a BH in a dynamical spacetime that has been ever carried out. In a follow up paper, we aim to present results from an expanded range of initial models, and to investigate in detail the dynamics of such systems, focusing on the development on the runaway instability, and the evolution of the BH due to the transfer of mass and angular momentum from the torus.

[1] L. Baiotti, B. Giacomazzo, and L. Rezzolla, arXiv:0804.0594.

[2] S. E. Woosley, Astrophys. J. **405**, 273 (1993).

[3] B. Paczynski, Astrophys. J. Lett. **494**, L45 (1998).

[4] Y. Sekiguchi and M. Shibata, Phys. Rev. D **70**, 084005 (2004).

[5] Y. Sekiguchi and M. Shibata, Prog. Theor. Phys. **117**, 1029 (2007).

[6] B. C. Stephens, M. D. Duez, Y. T. Liu, S. L. Shapiro, and M. Shibata, Class. Quantum Grav. **24**, S207 (2007).

[7] M. Shibata, M. D. Duez, Y. T. Liu, S. L. Shapiro, and B. C. Stephens, Phys. Rev. Lett. **96**, 031102 (2006).

[8] M. Shibata and K. Uryu, Phys. Rev. D **61**, 064001 (2000).

[9] M. Shibata, K. Taniguchi, and K. Uryu, Phys. Rev. D **68**, 084020 (2003).

[10] P. Marronetti, M. D. Duez, S. L. Shapiro, and T. W. Baumgarte, Phys. Rev. Lett. **92**, 141101 (2004).

[11] M. Shibata, K. Taniguchi, and K. Uryu, Phys. Rev. D **71**, 084021 (2005).

[12] M. Shibata and K. Taniguchi, Phys. Rev. D **73**, 064027 (2006).

[13] M. Shibata and K. Uryu, Phys. Rev. D **74**, 121503 (2006).

[14] M. Shibata and K. Uryu, Classical Quantum Gravity **24**, S125 (2007).

[15] T. Piran, Phys. Rep. **314**, 575 (1999).

[16] M. A. Aloy, E. Müller, J. M. Ibáñez, J. M. Martí, and A. MacFadyen, Astrophys. J. **531**, L119 (2000).

[17] M. A. Aloy and H. T. Janka, and E. Müller, Astron. Astrophys. **436**, 273 (2005).

[18] P. Meszaros, Rep. Prog. Phys. **69**, 2259 (2006).

[19] M. A. Abramowicz, M. Calvani, and L. Nobili, Nature (London) **302**, 597 (1983).

[20] J. A. Font and F. Daigne, Mon. Not. R. Astron. Soc. **334**, 383 (2002).

[21] F. Daigne and J. A. Font, Mon. Not. R. Astron. Soc. **349**, 841 (2004).

[22] J. A. Font, Living Rev. Relativity **6**, 4 (2003).

[23] S. Brandt and J. A. Font, *Proceedings of the 8th Marcel Grossmann Meeting on General Relativity*, edited by T. Piran (World Scientific, Singapore), pp. 744–746 1997.

[24] S. Brandt, J. A. Font, J. M. Ibáñez, J. Massó, and E. Seidel, Comput. Phys. Commun. **124**, 169 (2000).

[25] M. Campanelli, C. O. Lousto, P. Marronetti, and Y. Zlochower, Phys. Rev. Lett. **96**, 111101 (2006).

[26] J. G. Baker, J. Centrella, D. I. Choi, M. Koppitz, and J. van Meter, Phys. Rev. Lett. **96**, 111102 (2006).

[27] F. Pretorius, arXiv:0710.1338.

[28] J. A. Faber, T. W. Baumgarte, Z. B. Etienne, S. L. Shapiro, and K. Taniguchi, Phys. Rev. D **76**, 104021 (2007).

[29] L. Baiotti and L. Rezzolla, Phys. Rev. Lett. **97**, 141101 (2006).

[30] M. Shibata, Phys. Rev. D **76**, 064035 (2007).

[31] S. Nishida and Y. Eriguchi, Astrophys. J. **427**, 429 (1994).

[32] M. Ansorg and D. Petroff, Phys. Rev. D **72**, 024019 (2005).

[33] T. Nakamura, K. Oohara, and Y. Kojima, Prog. Theor. Phys. Suppl. **90**, 1 (1987).

[34] M. Shibata and T. Nakamura, Phys. Rev. D **52**, 5428 (1995).

[35] T. W. Baumgarte and S. L. Shapiro, Phys. Rev. D **59**, 024007 (1999).

[36] F. Banyuls, J. A. Font, J. M. Ibánez, J. M. Martí, and J. A. Miralles, Astrophys. J. **476**, 221 (1997).

[37] M. Shibata, Phys. Rev. D **67**, 024033 (2003).

[38] M. Alcubierre, S. Brandt, B. Brügmann, D. Holz, E. Seidel, R. Takahashi, and J. Thornburg, Int. J. Mod. Phys. D **10**, 273 (2001).

[39] M. Alcubierre, B. Brügmann, P. Diener, M. Koppitz, D. Pollney, E. Seidel, and R. Takahashi, Phys. Rev. D **67**, 084023 (2003).

[40] S. Brandt and B. Brügmann, Phys. Rev. Lett. **78**, 3606 (1997).

[41] D. Brill and R. Lindquist, Phys. Rev. **131**, 471 (1963).

[42] B. Brügmann, Int. J. Mod. Phys. D **8**, 85 (1999).

[43] M. Alcubierre, W. Benger, B. Brügmann, G. Lanfermann, L. Nerger, E. Seidel, and R. Takahashi, Phys. Rev. Lett. **87**, 271103 (2001).

[44] M. Campanelli, C. O. Lousto, Y. Zlochower, B. Krishnan, and D. Merritt, Phys. Rev. D **75**, 064030 (2007).

[45] J. G. Baker, S. T. McWilliams, J. van Meter, J. Centrella, D. I. Choi, B. J. Kelly, and M. Koppitz, Phys. Rev. D **75**, 124024 (2007).

[46] J. A. González, M. Hannam, U. Sperhake, B. Brügmann, and S. Husa, Phys. Rev. Lett. **98**, 231101 (2007).

[47] P. Marronetti, W. Tichy, B. Brügmann, J. González, and U. Sperhake, Phys. Rev. D **77**, 064010 (2008).

[48] L. Rezzolla, P. Diener, E. N. Dorband, D. Pollney, C. Reisswig, E. Schnetter, and J. Seiler, Astrophys. J. **674**, L29 (2008).

[49] D. Pollney, C. Reisswig, L. Rezzolla, B. Szilágyi, M. Ansorg, B. Deris, P. Diener, E. N. Dorband, M. Koppitz, A. Nagar, and Schnetter, Phys. Rev. D **76**, 124002 (2007).

[50] F. Herrmann, I. Hinder, D. M. Shoemaker, P. Laguna, and R. A. Matzner, Phys. Rev. D **76**, 084032 (2007).

[51] C. Bona, J. Massó, E. Seidel, and J. Stela, Phys. Rev. D **56**, 3405 (1997).

[52] M. Hannam, S. Husa, B. Brügmann, J. A. González, U. Sperhake, and N. OMurchadha, J. Phys. Conf. Ser. **66**, 012047 (2007).

[53] B. Brügmann, J. A. Gonzalez, M. Hannam, S. Husa, U. Sperhake, and W. Tichy, arXiv:gr-qc/0610128.

[54] J. van Meter, J. G. Baker, M. Koppitz, and D. I. Choi, Phys. Rev. D **73**, 124011 (2006).

[55] S. A. Teukolsky, Phys. Rev. D **61**, 087501 (2000).

[56] R. J. Spiteri and S. J. Ruuth, SIAM J. Numer. Anal. **40**, 469 (2002).

[57] Y. Zlochower, J. G. Baker, M. Campanelli, and C. O. Lousto, Phys. Rev. D **72**, 024021 (2005).

[58] W. H. Press, B. P. Flannery, S. A. Teukolsky, and W. T. Vetterling, *Numerical Recipes* (Cambridge University Press, New York, 1992).

[59] J. A. Font, T. Goodale, S. Iyer, M. Miller, L. Rezzolla, E. Seidel, N. Stergioulas, W. M. Suen, and M. Tobias, Phys. Rev. D **65**, 084024 (2002).

[60] M. Shibata, Phys. Rev. D **55**, 2002 (1997).

[61] J. Thornburg, Living Rev. Relativity **10**, 743 (2007).

[62] B. Imbiriba, J. Baker, D. Choi, J. Centrella, D. R. Fiske, J. D. Brown, J. R. van Meter, and K. Olson, Phys. Rev. D **70**, 124025 (2004).

[63] M. Hannam, S. Husa, D. Pollney, B. Brügmann, and N. OMurchadha, Phys. Rev. Lett. **99**, 241102 (2007).

[64] T. W. Baumgarte and S. G. Naculich, Phys. Rev. D **75**, 067502 (2007).

[65] J. M. Martí and E. Müller, J. Comput. Phys. **123**, 1 (1996).

[66] J. M. Martí and E. Müller, Living Rev. Relativity 1 (2003).

[67] J. M. Martí, E. Müller, J. A. Font, J. M. Ibáñez, and A.

Marquina, Astrophys. J. **479**, 151 (1997).

[68] M. A. Aloy, J. M. Ibáñez, J. M. Martí, and E. Müller, Astrophys. J. Suppl. Ser. **122**, 151 (1999).

[69] T. G. Cowling, Mon. Not. R. Astron. Soc. **101**, 367 (1941).

[70] J. A. Font, N. Stergioulas, and K. D. Kokkotas, Mon. Not. R. Astron. Soc. **313**, 678 (2000).

[71] L. Baiotti, I. Hawke, P. Montero, and L. Rezzolla, in *Mem. Soc. Astron. It.*, edited by R. Capuzzo-Dolcetta (2003), vol. 1, p. 327.

[72] N. Stergioulas and J. A. Font, Phys. Rev. Lett. **86**, 1148 (2001).

[73] O. Zanotti, L. Rezzolla, and J. A. Font, Mon. Not. R. Astron. Soc. **341**, 832 (2003).

[74] L. Rezzolla, S. Yoshida, and O. Zanotti, Mon. Not. R. Astron. Soc. **344**, 978 (2003).

[75] P. J. Montero, L. Rezzolla, and S. Yoshida, Mon. Not. R. Astron. Soc. **354**, 1040 (2004).

[76] O. Zanotti, L. Rezzolla, J. A. Font, and P. J. Montero, Mon. Not. R. Astron. Soc. **356**, 1371 (2005).

[77] P. J. Montero, O. Zanotti, J. A. Font, and L. Rezzolla, Mon. Not. R. Astron. Soc. **378**, 1101 (2007).